Preparation and characterization of Cu2ZnxFe1–xSnS4 thin films deposited on intrinsic silicon substrates

Marwa Sebai, Ghada Bousselmi, Jean-Louis Lazzari, Mounir Kanzari

Preparation and characterization of $Cu_2Zn_xFe_{1-x}SnS_4$ thin films deposited on intrinsic silicon substrates

Marwa Sebai [a,*], Ghada Bousselmi [a], Jean-Louis Lazzari [b], Mounir Kanzari [a,c]

[a] Université de Tunis El Manar, Ecole Nationale d'Ingénieurs de Tunis, Laboratoire de Photovoltaïque et Matériaux Semi-Conducteurs, 1002, Tunis, Tunisia
[b] Aix Marseille Univ, CNRS, CINAM, Case 913, Campus de Luminy, Marseille, France
[c] Université de Tunis, IPEITunis Montfleury, Laboratoire de Photovoltaïque et Matériaux Semi-conducteurs-ENIT, Tunisia

ARTICLE INFO

Keywords:
Thin film
Thermal evaporation
Structural properties
Elemental composition
Impedance spectroscopy
AC conductivity

ABSTRACT

The present paper reports the study of the effect of zinc content in $Cu_2Zn_{1-x}Fe_xSnS_4$ thin films. To achieve this purpose, CZTS, $CZ_{0.5}F_{0.5}TS$ and CZTS thin films were grown at room temperature via thermal evaporation on unheated silicon substrates, which was followed by sulfidation at 400 °C. Analysis by x-ray diffraction indicates the polycrystalline nature of the CZFTS films with a preferential orientation along the (112) plane with structural transition from stannite (x = 0) to kesterite (x = 1) as the zinc content increases. The elemental composition of all thin films was analyzed by the EDAX technique. Morphological patterns were also explored in order to better understand the evolution of grain size and thickness as a function of zinc content. Hall effect measurements showed that the highest conductivity was obtained for CZTS. Impedance spectroscopy (IS) was performed between 5 Hz and 13 MHz. The complex impedance plots of the different samples revealed a single semicircle, suggesting that the response comes from a single capacitive element consistent with the grains. This measurement (IS) confirmed the enhancement of the conduction mechanism with increasing x-fraction. Experimental data suggested that AC conductivity in thin films C(Z, F)TS is proportional to ω_s ($s < 1$). This is consistent with the correlated barrier hopping (CBH) model.

1. Introduction

Over the last few decades, the study of absorber materials for thin film photovoltaic (PV) cells has become a major focus in order to improve the cost efficiency of solar production and, in particular, to reduce the cost of raw materials [1]. Initial research focused on CdTe and $CuIn_{1-x}Ga_xSe_2$ based absorber materials [2]. However, toxicity of cadmium and low availability of Indium (In), Gallium (Ga) and Tellurium (Te) have resulted in the need for new materials that are abundant and non-toxic [3,4]. Among the most widely explored alternatives to CIGS are Cu_2ZnSnS_4 (CZTS) and Cu_2FeSnS_4 (CFTS), which contain relatively abundant and cost-effective components, namely Zn, Fe and Sn, instead of Ga and In. Two main crystal structures can be distinguished, the most stable being kesterite (CZTS) and stannite (CFTS). In addition, the high value of the absorption coefficient above 10^4 cm^{-1} and the direct band gap between 1.4 and 1.5 eV and between 1.2 and 1.4 eV, respectively, make them particularly appropriate for solar cell industry applications [5]. The two structures are considered to be quite similar, although they differ in the distribution of Cu^{+1}, Zn^{+2} and Fe^{+2} cations [6,7]. Furthermore, it is often reported that the optical band gap of C(Z, F)TS decreases from 1.5 to 1.2 eV with increasing iron content [8,9]. However, the efficiency of CZTS and CFTS thin film solar cells stands currently at 5 % and 12.6 %, respectively [10,11]. The literature up to 2014 for the material $Cu_2Zn_{1-x}Fe_xSnS4$, C(Z,F)TS reported that the transition from kesterite to stannite occurs with about 40 % iron [12,13]. Since 2016, Shadrokh et al. [4] reported that the phase transition from kesterite to stannite occurs with 60 % iron. Physical vapour deposition (PVD) techniques have proven to be very suitable for the production of C(Z, F)TS solar cells, although they do require heat treatment in a sulphur vapor atmosphere for the production of a pure polycrystalline phase [14]. C(Z, F)TS thin films technology has been applied in many fields including sensor transducers, electronic components, high temperature corrosion resistance, solar cells and thermal insulation [14]. According to the literature, the structural properties of CZFTS thin films depend on the substrate type, whether deposited on an amorphous insulating substrate such as glass, which is the most common

* Corresponding author.
E-mail addresses: Sebai.marwa11@gmail.com (M. Sebai), bousselmighada@gmail.com (G. Bousselmi), jean-louis.lazzari@cnrs.fr (J.-L. Lazzari), mounir.kanzari@ipeit.rnu.tn (M. Kanzari).

https://doi.org/10.1016/j.mtcomm.2023.105558

substrate, or on a monocrystalline substrate such as silicon [12,14,15]. Most CZFTS investigations are directed toward the synthesis of nanoparticles, which are subsequently applied as thin films. However, these films mostly struggle with poor surface adhesion and irregular particle formation. To overcome these limitations, coating techniques and conditions, as well as the nature of the substrate, should be carefully optimized in order to achieve compact and uniform thin films with high efficiency.

In the present study, we propose to evaluate $CZ_{0.5}F_{0.5}TS$ thin films from a mixture of 50 % iron and 50 % zinc, CZTS and CFTS deposited on pure intrinsic silicon substrates. In fact, the implementation of CZTS thin films on a silicon substrate has attracted considerable focus in the design of the CZTS/Si tandem cell [16]. This study was based on the modelling of a wide bandgap CZTS sub-cell on a narrow bandgap silicon sub-cell, separated by TiN, which represents the front contact of the lower sub-cell. According to this investigation, tandem cells allow the solar spectrum to be spread over several sub-cells with different band gaps to better convert sunlight into electricity compared to single junction solar cells. The effect of direct deposition of CFTS, CZFTS and CZTS powders on pure intrinsic silicon wafers on crystal growth, surface morphology and electrical properties was investigated in this work.

2. Experimental details

2.1. Synthesis of $Cu_2(Zn, Fe)SnS_4$ ingots

$Cu_2(Zn, Fe)SnS_4$ ingots were synthesized by direct melting. The high purity (99.999 %) elemental components, copper (Cu), zinc (Zn), iron (Fe), tin (Sn) and sulphur (S) were carefully picked out by stoichiometric composition [17]. They were subsequently placed in a quartz tube. The individual tubes were sealed under vacuum (10^{-6} Torr) and then placed in a horizontal position in a programmable furnace (Nabertherm-Germany). A suitable thermal profile was maintained to form $Cu_2(Zn, Fe)SnS_4$ ingots. Finally, they were ground to obtain powders (Fig. 1).

2.2. $Cu_2(Zn, Fe)SnS_4$ thin films preparation

In this work, a vacuum thermal evaporation technique was adopted to develop $Cu_2(Zn, Fe)SnS_4$ thin films [17]. The deposition was performed in a vacuum chamber (Alcatel unit) in which the pressure was around 10^{-6} Torr. C(Z, F)TS powders were used as targets for a molybdenum crucible. The deposition was performed at room temperature on clean intrinsic silicon substrates with a preferred orientation of (001), having a thickness between 250 and 300 µm and a resistance ranging between 250 and 350 Ω. In order to improve the crystallinity of the films, the $Cu_2Zn_xFe_{1-x}SnS_4$ thin films were sulphided under nitrogen flow at 400 °C for 30 min. The use of nitrogen allowed for minimal oxidation while sulfur was used in this annealing to avoid the defects encountered.

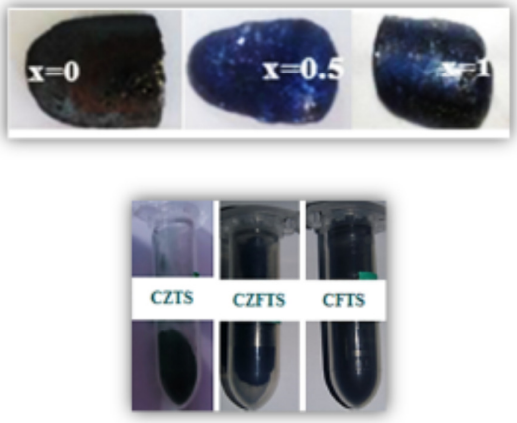

Fig. 1. Ingots and powders of as-synthesized $Cu_2Zn_xFe_{1-x}SnS_4$ (x = 0; 0.5; 1).

2.3. Characterisation

A structural study was performed using an X-ray diffractometer (Xpert Pro PANalytical) in a 2θ range from 20° to 70° with CuKα radiation of (λ = 1.5406 Å). Similarly, Raman analysis was conducted using (Horiba Jobin Yvon Lab-RAM) with an excitation wavelength of 432 nm at room temperature. Morphological investigations were performed by scanning electron microscopy (SEM), fixed by an energy dispersive X-ray spectroscope (EDS). The surface topographies of the films were investigated by atomic force microscopy (AFM), using a tapping (Veeco Dimension AFM), in tapping mode. The optical measurement was studied by a profilometer to investigate the thickness progression in the CZFTS formula. The electrical properties were determined by Hall Effect analysis in the Van Der Paw configuration using an Ecopia AMP55T. Electrical conductivity of post-sulfide thin films were studied using an HP4192A impedance analyzer in the frequency range of 5 Hz to 13 MHz. The configuration of the electrical measurements was done through two electrodes, coated on both ends of the sample using a silver paste.

3. Results and discussion

3.1. Structural and morphological study of CZFTS powders

3.1.1. Phase structure analysis

XRD diffraction patterns display that all C(Z, F)TS powders are polycrystalline and show clearly distinct diffraction peaks suggesting good crystallinity and homogeneity (Fig. 2). The main peaks found at 2θ = 28.57°, 32.96°, 47.58° and 56.22° for CFTS (JCPDS card no: 00-044-1476) and 2θ = 28.51°, 33.06°, 47.37° and 56. 20° for CZTS (JCPDS card no: 00-026-0575), which correspond to the (112) (200) (220)/(204) and (312)/(116) planes of the polycrystalline stannite CFTS and the kesterite CZTS. According to previous studies, the Cu_2ZnSnS_4 material is energetically more stable in the kesterite structures than in the stannite structure [18]. Additionally, a few small peaks located at 32.02° can be observed for CZTS corresponding to the (004) plane of the SnS phase (JCPDS file no: 00-053-00526). With increased Fe content, the dominant peak (112) shifts slightly to higher angles. Such variations have been reported in other research [19] and can be correlated to the small radius difference between Fe^{2+} (0.66 Å) and Zn^{2+} (0.64 Å) and the transition phase from stannite to kesterite [20,21]. In order to understand the effect of Zn content on the structural properties of CZFTS powders, the lattice parameters 'a' and 'c' of CFTS, $CZ_{0.5}F_{0.5}TS$ and CZTS powders are estimated using the relation for the tetragonal structure:

$$\frac{1}{d^2} = \frac{h^2 + k^2}{a^2} + \frac{l^2}{c^2} \quad (1)$$

Where h, k and l are the Miller indices corresponding to the XRD peaks and d_{hkl} is the inter-planar spacing calculated according to the well-known Bragg relation:

$$2d_{hkl}\sin\theta = n\lambda \quad (2)$$

To study the structural transition in the C(Z, F)TS semiconductor, we estimated the tetragonal disorder parameter η=c/2a. This parameter affects the electronic structure in chalcopyrite materials significantly and is defined as the deviation of the ratio of the major axis 'c' to twice the minor axis from c/2a = 1 [22]. Table 1 shows the calculated lattice

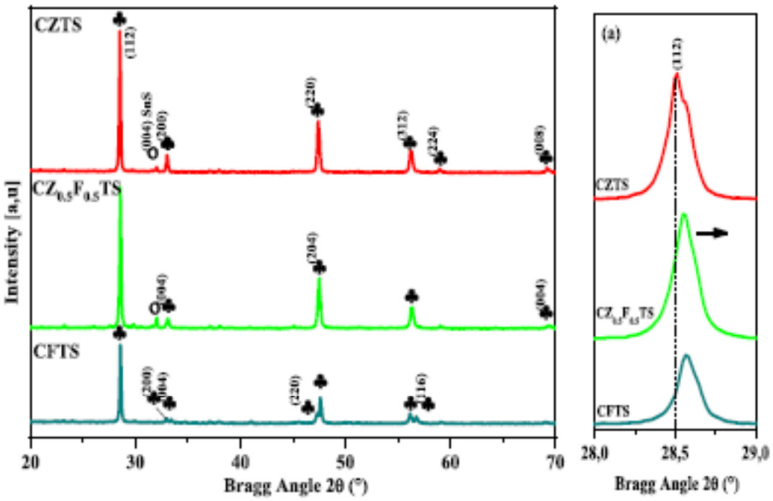

Fig. 2. XRD patterns of as-synthesized $Cu_2Zn_xFe_{1-x}SnS_4$ (x = 0; 0.5; 1) powders, and (a) variation of (112) plane.

Table 1
Lattice parameters (a and c), distortion parameter and unit cell volume of $Cu_2Zn_xFe_{1-x}SnS_4$ (x = 0; 0.5 and 1) compounds.

	$2\theta_{(112)}$ (°)	a ± 0.03 (Å)	c ± 0.03 (Å)	$\eta=\frac{c}{2a}$	V ± 0.03 (Å^3)
X = 0	28.57	5.43	10.72	0.986	316.08
X = 0.5	28.55	5.41	10.84	1.001	317.26
X = 1	28.51	5.42	10.82	0.997	317.85

parameters, distortion parameters and unit cell volume. The lattice parameters obtained are very similar to those reported in the standard PDF maps used for XRD indexing and in previous work. [19,20,23,24], with a small variation due to the different processing methods. Lattice parameter 'a' (Fig. 3, Table 1) decreases with increasing zinc content (x from 0 to 0.5) and then increases for x = 1, unlike lattice parameter 'c'. The discontinuity of these lattice parameters have already been reported in the literature and can be attributed to the structural transition between the stannite and kesterite phase that occurs around x = 0.5. This is expected to be due to the rearrangement of Cu^{+1}, Zn^{2+} and Fe^{2+} cations in the unit cell. The slightly small radius of Zn^{2+} (0.64 Å) substituted by Fe^{2+} (0.66 Å) and the rearrangement of Cu^{+1}, Zn^{2+} and Fe^{2+} cations [23,24].

Furthermore, T. Shibuya et al. found that the phase transition from kesterite to stannite occurs at about x = 0.4 for $Cu_2Zn_{1-x}Fe_xSnS_4$ [25].

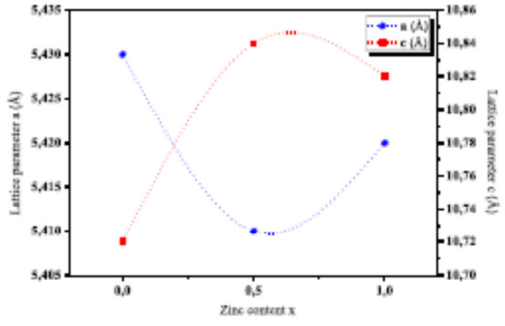

Fig. 3. Variation of lattice parameters a and c of $Cu_2Zn_xFe_{1-x}SnS_4$ (x = 0; 0.5 and 1) powders.

Furthermore, we can note that the c/2a ratio is very close to 1 which affirms the tetragonal system. It has already been reported in the literature that η is less than unity for the kesterite CZTS and stannite CFTS structures, which confirms our results [18,19].

Furthermore, the small variation in the distortion parameter could be attributed to the cation order in the sub-lattices between the two structures, which crystallize in different space groups. In the CZTS material with kesterite structure, for example, cation layers alternate with sulphur anion layers along the crystallographic c-direction, such as CuZn/SS/CuSn/SS, while in the stannite structure, CuCu/SS/FeSn/SS results in a small tetragonal distortion [19,22–24].

However, it can be pointed out that the volume of the unit cell increases with decreasing Fe content. This problem has been discussed in previous works and was mainly due to the redistribution of cations in the crystal lattice, which confirms the presence of covalent bonds in these compounds [19,23,24]. The crystallite size of the CZFTS powders was estimated from the basic Scherrer equation [26]:

$$D = \frac{0.9\lambda}{\beta\cos\theta} \tag{3}$$

D presents the average crystallite size, λ is the x-ray diffraction wavelength (in nm). β is the width of the X-ray peak (112) on the 2θ axis, taken as the total width at half maximum (FWHM) after the error due to instrumental broadening has been properly corrected (variance subtraction), θ is the Bragg angle and, through this paper [27]. The dislocation density (δ_{dis}), number of crystallites (N_c) per unit area and the strain (ε) are calculated by the following equations [28,29]:

$$\delta_{dis} = \frac{1}{D^2} N_c = \frac{1}{D^3}\varepsilon = \frac{\beta\cos\theta}{4} \tag{4}$$

The dislocation density δ_{dis} is defined as the length of the dislocation lines per unit volume of crystal, the lattice strain ε is defined as the disarrangement of lattice created during deposition process.

Table 2
Estimated values of the grain size (D), the full width at half-maximum (FHWH), dislocation density (δ_{dis}), the number of crystallites (Nc) per unit area and the strain (ε) of C(Z,F)TS powders.

	D (nm)	FWHM (°)	δ_{dis} (10^{-3} nm^{-2})	N_c (10^{-3} nm^{-2})	ε (10^{-2})
X = 0	54.6	0.156	1.225	0.0429	3.77
X = 0.5	48.9	0.154	1.226	0.0429	3.73
X = 1	51.2	0.150	1.230	0.0431	3.63

Table 2 summarizes the calculated values of D, β, δ_{dis}, Nc and ε of C(Z, F)TS powders. The higher crystallite size enhances the carrier diffusion length and reduces the carrier recombination in the grain boundaries, leading to an improvement in the conversion efficiency of solar cells based on CZTS as an absorber material [30]. Moreover, the lowest dislocation density (δ_{dis}), crystallite number per unit area (Nc) and strain (ε) obtained for CZTS thin films indicates that CZTS exhibit the best crystallinity.

3.1.2. Morphological study

Fig. 4 shows the SEM observations of $Cu_2Zn_{1-x}Fe_xSnS_4$ compounds (x = 0, 0.5, 1). It can be clearly distinguished that the incorporation of Zn in $Cu_2Zn_{1-x}Fe_xSnS_4$ compounds affects the surface morphology of the powders. Moreover, we can identify that with increasing the amount of Zn in the compound, the surface morphology of the CZFTS powder becomes bright due to the effect of Zn incorporation. Nevertheless, in all cases, a tendency towards compactness independently of the zinc content is noticed, especially for x = 1 which denotes the presence of large clusters.

3.2. Structural, surface morphological and electrical properties of C(Z, F)TS thin film

3.2.1. Composition analysis

The atomic ratio of the elements and the experimental composition of the C(Z,F)TS thin films were further evaluated by EDS analysis (Fig. 5 and Table 3). This analysis confirmed the presence of constituent elements in each material as shown in Table 3. However, CFTS thin film has been found to be deficient in sulphur and rich in copper. The composition of this material is therefore almost stoichiometric. On the other hand, EDS analysis revealed that the $Cu_2Zn_{0.5}Fe_{0.5}SnS_4$ thin film deviates from stoichiometry. This composition exhibits high copper and zinc content with a slight loss of sulphur, which could be the origin of secondary phases such as CuS, SnS and ZnS. CZTS presents a chemical composition close to stoichiometry.

3.2.2. Structural study

The X-ray diffraction (XRD) patterns of $Cu_2Zn_{1-x}Fe_xSnS_4$ thin films (x = 0; 0.5; 1) presented in Fig. 6 show that all the CZFTS thin films are polycrystalline and exhibit clear and distinct diffraction patterns, indicating good crystallinity and homogeneity. The CFTS (x = 0) exhibit major peaks detected at 28.48°, 33.01°, 47.44°, 56.37° and 61.70° associated with (112), (200), (204), (116) and (321) reticular planes corresponding to the stannite structure (JCPDS sheet N: 00-044-1476).

From the X-ray diffraction (XRD) patterns of CZTS, a prominent peak at 2θ= 28.56° corresponding to the (112) plane is highlighted. Similarly, several peaks are visible based on the (110), (103), (200)/(004), (202), (211), (114), (105), (220), (312) and (224) lattice planes. A minor peak can also be assigned to the secondary phase of the ZnS layer (JCPDS #00-036-1450) [31]. For x = 0.5, it is also noted the appearance of peaks corresponding to the stannite/kesterite structures of CFTS and CZTS respectively, with the presence of minority peaks that can be attributed to the ZnS secondary phases [31], SnS (JCPDS card n° 01-089-2028) [32] and SnS_2 (JCPDS card n° 00-039-0354) [33].

The crystallite size D_{D-S} of CZFTS thin films is calculated from the most intense (112) by using Scherer's formula [34] and then dislocation density (δ_{dis}), number of crystallites (N_c) per unit area and strain (ε) are also calculated [35,36].

Table 4 shows a summary of the calculated values of D, β, δ_{dis}, N_c, and ε of C(Z, F)TS thin films. Based on the findings reported in this Table, it can be observed that the values of the crystallite size D found by this study are higher than those found in other investigations. This may be explained by the homogeneity of the deposit and the good crystallization of the materials deposited on the Silicon substrates. It has been shown that silicon substrates provide a good adhesion of the materials deposited on them [37].

The lowest crystallite size value is obtained for $CZ_{0.5}F_{0.5}TS$. Indeed, as a result of the change in composition, the incorporation of different

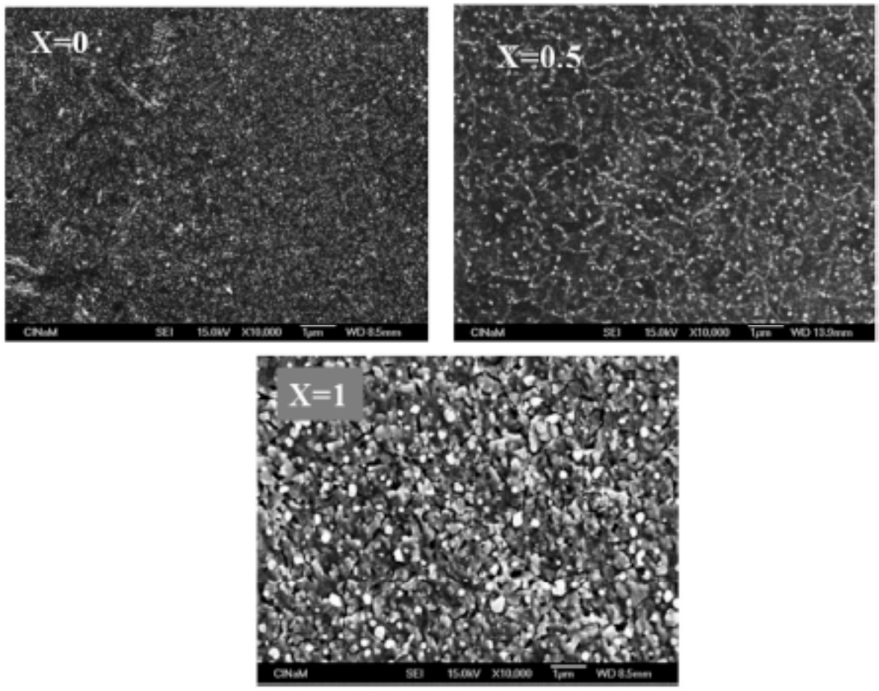

Fig. 4. SEM images of as-synthesized $Cu_2Zn_xFe_{1-x}SnS_4$ (x = 0; 0.5; 1) powders.

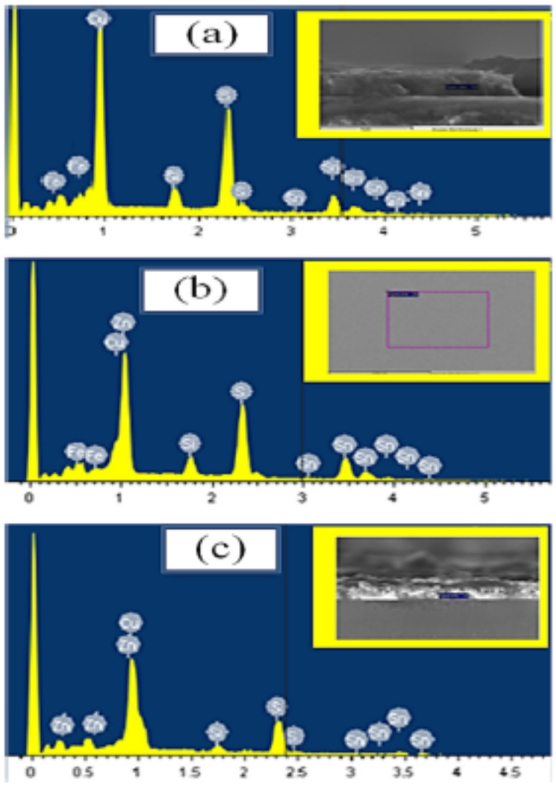

Fig. 5. EDS spectrum of (a) CFTS, (b) $CZ_{0.5}F_{0.5}TS$ and (c) CZTS thin films deposited on Si-intrinsic substrates.

ionic radius ions (substitution of Fe^{2+} (0.66 Å) by Zn^{2+} (0.64 Å) leads to a competition between the two ions in order to occupy the same position in the crystalline structure. This will increase the disorder and the deformation inside the unit cell, leading to the decrease of the crystalline quality and thus of the crystallite size. The highest crystallite size D obtained for the CZTS thin films was 113 nm. It should be noted that the largest value of crystallite size obtained is consistent with the good crystal structure of the CZTS thin films. The same result was previously published by Jiang et al. [38]. Basically, the larger crystallite size increases the carrier diffusion distance and decreases the carrier recombination at grain boundaries, which ultimately leads to an improvement in the conversion efficiency of solar cells based on CZTS as an absorber material. Furthermore, the lowest dislocation density (δ_{dis}), number of crystallites per unit area (Nc) and strain (ε) were obtained for CZTS thin films, resulting in better crystallinity of CZTS.

3.2.3. Raman spectroscopy

Due to the similarity of CZTS peaks with binary and ternary phases, the XRD technique cannot distinguish between the different phases. Therefore, Raman spectroscopy was performed to confirm the presence of this material by identifying its vibrational modes (Fig. 7). It can be seen that the majority of the peaks are attributed to the Cu2ZnSnS4 phase, with the presence of a significant peak at 337 cm^{-1}, which corresponds perfectly to the A mode of the kesterite structure [39]. The presence of this strong band indicates the complete incorporation of the atoms into the structural lattice and the homogeneous formation of the CZTS [39]. Several vibrational modes are also observed at 285 cm^{-1}, 305 cm^{-1}, 331 cm^{-1} and 367 cm^{-1} respectively, confirming the polycrystalline nature of the material.

In addition, the peaks identified at 260 cm^{-1} and 354 cm^{-1} are attributed to the Zn-S vibration mode [40,41]. These investigations confirm the XRD results and are in good agreement with those reported by different authors, Table 5.

3.2.4. Morphological properties

In order to understand the transition process between the stannite and kesterite phases, the morphology of CZFTS was investigated by scanning electron microscopy (SEM) and atomic force microscopy (AFM, tap mode).

Fig. 8 shows the morphological structure of the deposited $CZ_xF_{1-x}TS$ films for $0 < x < 1$. Accordingly, we can see that the SEM images are formed by small crystallites and the layers are compact and uniform [45]. By increasing the Zn precursor in the mixture, a clear improvement in the particle size is observed, especially at $x = 0.5$. The remarkable difference found in the SEM images of $CZ_{0.5}F_{0.5}TS$ compared to the other films is reflected by small grains adhering to flakes irrigated in the form of thick hexagonal plates. It is possible that this phenomenon is due to the mixing of two different crystalline structures, stannite CFTS and kesterite CZTS, in the alloyed CZFTS films [46] and/or to the deposition of p-type semiconductors on intrinsic silicon substrates with a (001) preferred orientation. Fig. 8(a and b) clearly shows the obtained morphology of the $CZ_{0.5}F_{0.5}TS$ thin films. In addition, the SEM image of CZTS illustrates the formation of large grains compared to CFTS. The surface morphology is inhomogeneous with smooth islands separated by rough regions; this surface is formed by the aggregation of clustered aggregates. This increase in grain size is strongly related to the increase in crystallite size, decrease in grain boundary and improved crystallinity of the CZTS material. It has also been reported that the conversion efficiency of CZTS films in a solar cell is strongly related to grain size, as a large grain size absorber layer maximizes the minority carrier diffusion length and the intrinsic potential of a polycrystalline solar cell [47].

The cross-sectional image for CFTS, $CZ_{0.5}F_{0.5}TS$ and CZTS reveals well crystalized and compact grains, Fig. 8(a, b and c) [45]. Notably, all films have approximately similar thickness with a slight improvement from CFTS to CZTS resulting from the increase in grain size. A similar result has been reported in the literature [17]. The grain size and thickness obtained from SEM and cross-sectional image of C(Z, F)TS films are shown in Table 6. The derived values obtained for the grain size are in close agreement with those derived from the crystallite size.

Atomic force microscopy (AFM) analysis provides surface visualization and he average roughness measurements of films deposited on a surface (2 μm _ 2 μm) in contact mode. Three-dimensional (3D) and two-dimensional (2D) AFM micrographs of C(Z, F)TS deposited on intrinsic silicon substrates are shown in Fig. 9. Table 6 lists the root mean square (RMS) values of the mean surface roughness. From the 3D AFM analyses, the CFTS thin film shows a uniform topography and thickness, the surface is smooth, homogeneous and the grains are dense with different

Table 3
Elemental composition of $Cu_2Zn_xFe_{1-x}SnS_4$ (x = 0; 0.5; 1) thin films.

Theoretical Composition	Element [at%]					Experimental Composition
	Cu	Zn	Fe	Sn	S	
Cu_2FeSnS_4	29.67	0	11.14	13.89	45.37	$Cu_{2.37}Fe_{0.64}Sn_{1.11}S_{3.62}$
$Cu_2Zn_{0.5}Fe_{0.5}SnS_4$	27.82	7.22	5.31	12.53	47.12	$Cu_{2.22}Zn_{0.57}Fe_{0.42}Sn_1S_{3.76}$
Cu_2ZnSnS_4	25.38	10.87	0	15	48.75	$Cu_{2.03}Zn_{0.87}Sn_{1.2}S_{3.9}$

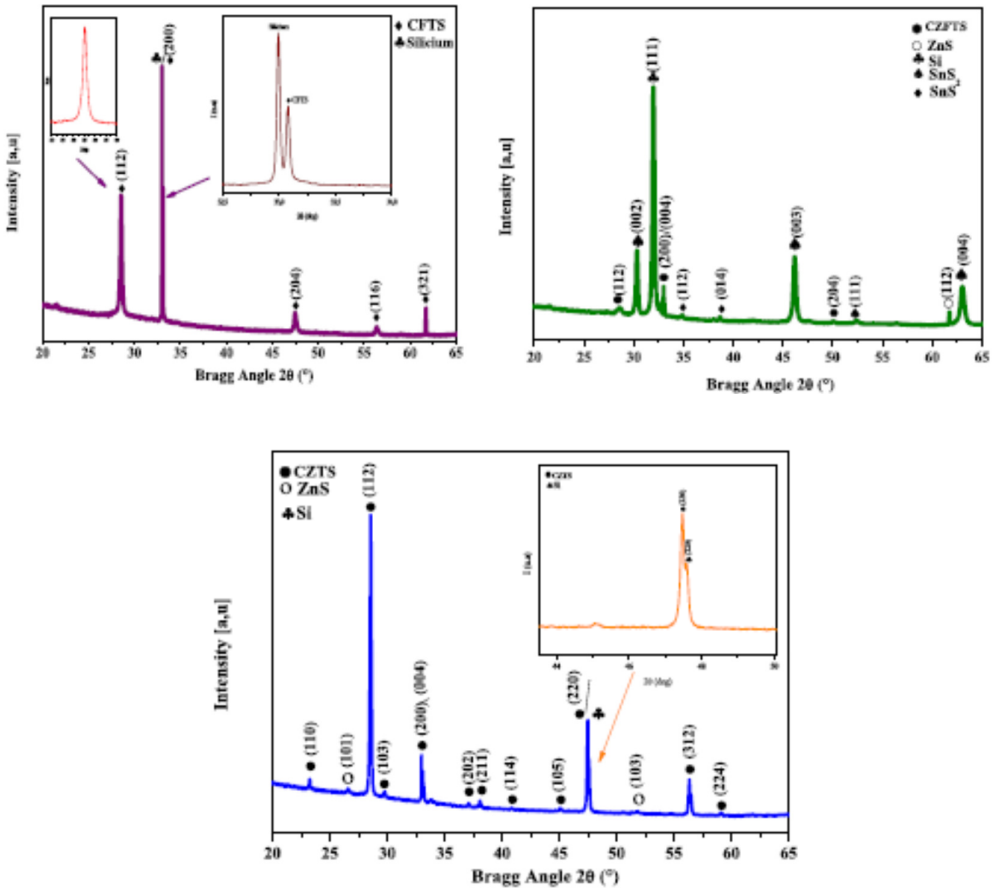

Fig. 6. XRD patterns of $Cu_2Zn_8Fe_{1-x}SnS_4$(x = 0, 0.5, 1) thin films.

Table 4
Estimated values of the full width at half-maximum (FHWH), grain size (D), dislocation density (δ_{dis}), the number of crystallites (Nc) per unit area and the strain (ε) of C(Z,F)TS thin films.

	Plan	2θ	FWHM (°)	D (nm)	δ_{dis} (10^{11} cm^{-2})	N_c (10^{11} cm^{-2})	ε
CFTS	(112)	28.48	0.21	75	0.17	0.62	0.05
$CZ_{0.5}F_{0.5}TS$	(112)	28.55	0.73	22	2.06	3.09	0.17
CZTS	(112)	28.56	0.14	113	0.078	0.025	0.03

sizes distributed over the surface of the film. The AFM image of $CZ_{0.5}F_{0.5}TS$ shows irregular grain clusters and higher surface roughness, which confirms the micrographic analysis obtained by SEM. Furthermore, for the CZTS thin film, agglomerated particle dispersion on the surface is observed [48].

3.2.5. Variations in film thickness

To investigate the effect of varying the zinc content in the CZFTS composition, the thickness of the materials was measured using a profilometer. Table 6 presents the corresponding results of thickness measurements of C(Z,F)TS films deposited on intrinsic silicon. This table clearly illustrates that increasing the percentage of zinc in $Cu_2Zn_8Fe_{1-x}SnS_4$ from 0 to 1 also leads to an increase in film thickness. This confirms previous results obtained with similar materials [17]. It is therefore suggested that the transition between the stannite and kesterite phases is responsible for the increase in thickness, which is in strong agreement with the morphological result.

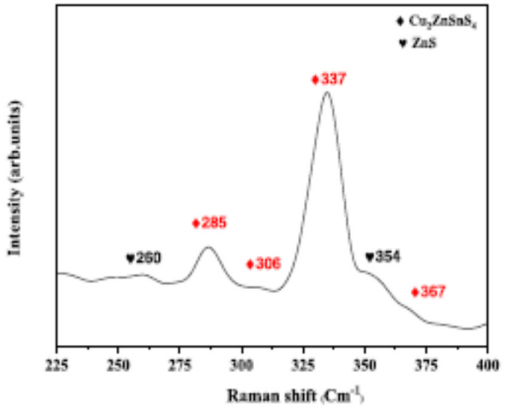

Fig. 7. Raman spectrums of CZTS thin films.

Table 5
The experimental values obtained by Raman spectroscopy with those reported by other authors.

This work (Cm^{-1})	Further work			
260	262 [40]	252 [41]		
285	285 [39]	286 [41]	287 [40]	281.7[43]
306	306 [39]	302 [40]	309 [44]	
331	331 [40]	331.5 [42]	332.7 [44]	
337	337 [39]	337.5 [40]	338.5 [43]	335.2 [44]
354	354.8 [44]	352 [39]	357 [43]	
367	366 [40]	365.3 [43]		

3.2.6. *Electrical properties*

In order to confirm the conductivity type of C(Z, F)TS, the hot probe method was adopted. P-type conductivity was found for CFTS, $CZ_{0.5}F_{0.5}TS$ and CZTS materials. Since p-type semiconductors are used, the conductivity is provided by the holes. In fact, the holes can move freely in the solid, jumping from atom to atom, from near to near. They act as charge carriers that circulate in the solid and allow the current to flow. I-V curves of the samples were highlighted under normal luminescence. All the samples presented an almost linear and symmetrical current-voltage curve at the origin. With increased voltage, the current increases linearly, suggesting the ohmic nature of the silver paste/CZFTS contacts (Fig. 10). With this excitation, the valence band holes can be stimulated, leading to an increase in the conductivity of the sample. This photo response behavior suggests the potential of exploiting CZFTS nanocrystals under thermal vacuum evaporation as an absorbing layer in solar cells.

3.2.6.1. Hall measurements. In the present study, intrinsic silicon substrates with a resistance between 250 and 350 Ω and a gap energy of 1 eV with a preferred orientation (001) were adopted. The synthesized thin films were annealed in a sulphide atmosphere under nitrogen flow. It should be noted that these parameters have a strong influence on the electrical properties of the developed materials. In order to better understand the effect of these parameters on the electrical properties of C (Z, F)TS films, Hall effect measurements were carried out. The results obtained are shown in Table 7.

Dhruba B.et.al [49] carried out the annealing of CFTS thin films under a sulphur gas atmosphere and found a higher electrical mobility after this process. They explained the change in μ by the ionisation of intrinsic donor and acceptor defects, which generate electrons and holes respectively, and thus the large population of intrinsic defects leads to a higher carrier concentration in the films, affecting the carrier mobility [50].

The Hall Effect measurements revealed a p-type conductivity for all materials. In stoichiometric CZTS, oxidation states of Cu, Zn, Sn and S are +I, +II, +IV, and −II, respectively. However, due to multivalancy of Sn it can exist in both +II and +IV oxidation states. In fact it is well known that tin based antisite defects acts as donor defects and serve to compensate the available most probable acceptor defects such as CuZn and VCu present in the system. However, there is a high probability of Sn at Zn site because of lower formation energy of Sn_{Zn}^{2+} in CZTS [51]. The conductivity of Cu_2ZnSnS_4 (CZTS) is in agreement with the theoretical reports suggesting that conductivity increases with increase in Cu/Sn ratio in CZTS samples [52]. Therefore, it appears that the ion tin Sn^{4+} plays an important role in the conductivity of the Cu_2XSnS_4 compounds.

As can be seen from the Table 7, the mobility values obtained are much higher than those reported for the CFTS and CZTS thin films [49, 53]. Indeed, the absence of secondary phases increases carrier mobility, further reducing resistivity and thus improving the overall electrical properties obtained for CZTS and CFTS thin films. Similarly, the lowest resistivity values are obtained for the CZTS thin films. This may be due to the better crystalline quality associated with the increased grain size (confirmed by SEM) and the intensity of the preferential orientation. Mustafa Ozta et.al [54] state that an increase in the average grain size leads to a decrease in the grain boundary zones. Consequently, these structural changes may contribute to the reduction in electrical resistivity. $CZ_{0.5}F_{0.5}TS$ showed the lowest mobility (this can be explained by its surface morphology, the growth of nanoflakes reduces the electron transfer and therefore their mobility). Furthermore, it has been previously observed that the mobility of the charge carriers is strongly dependent on the microstructure and the secondary phase, such as SnS_x and ZnS [55]. Hall measurements performed on C(Z, F)TS showed a high values of carrier concentration and resistivity compared to previous studies [49,53], this may be explained by the fact that we have deposited a p-C(Z, F)TS on a resistive intrinsic silicon.

3.2.6.2. Impedance spectroscopy. In order to properly understand the interactions between spins and ions, the magnetic properties and the electrical properties of CZFTS thin films, some deep investigations must be carried out [56–59]. In this section, we focus on the study of the electrical properties of CZFTS thin films by the electrical impedance spectroscopy technique IS.

IS technique provides useful information for improved control of the relaxation process and for correlating electrical properties with material structure [60]. Despite the importance of studying the electrical properties of semiconductors using the impedance spectroscopy technique, few studies have been carried out using this technique on CZFTS thin films. In fact, this method is mainly characterized by the application of a sinusoidal current V(t) to recover the value of the current I(t). The resulting materials were subjected to complex impedance studies at varying frequencies and temperatures to evaluate their corresponding electrical conductivity.

Fig. 11 displays the complex impedance spectra (Z'' versus Z') obtained by tracing the imaginary versus real part of post-sulphurized $Cu_2Zn_xFe_{1-x}SnS_4$. A single semicircular arc is detected for all temperatures. It can therefore be suggested that the grains dominate the conduction process [61].

In addition, a decrease in the diameter and maximum of all the circular arcs is clearly noticeable with increasing temperature, suggesting a decrease in their electrical resistivity and thus an increase in electrical conduction in these materials [61]. Such results are evidence of the semiconducting behaviour of these samples. It can be assumed that the electrical conduction is thermally activated [61]. In addition, the diameter and maximum of the semicircles for CFTS, $CZ_{0.5}F_{0.5}TS$ and CZTS increase with increasing zinc content from $3.5 \times 10^3\ \Omega$ for CFTS to $3.5 \times 10^5\ \Omega$ for CZTS. This variation could be attributed to the change in crystalline structure.

The complex impedance of each arc is given by [62]:

$$Z(\omega) = R/(1 + j\omega RC) \quad (5)$$

Indeed, for CFTS, $CZ_{0.5}F_{0.5}TS$ and CZTS materials, the response of the sample following the application of an electric field is seen. This response can be associated with the intergranular polarization mechanism appearing at higher frequencies. The arc maximum was characterized by an angular frequency maximum described by a constant time or characteristic relaxation time $\tau = RC = 1/\omega_m$, where ω_m is the maximum angular pulsation. Moreover, with the presence of semicircles, it is possible to demonstrate the homogeneity of post-sulfurized C(Z, F)TS thin films. Such characteristics are in accordance with the morphological and structural analysis.

The relaxation time can be evaluated by plotting Z'' as a function of frequency at different annealing temperatures. Fig. 12 illustrates the variation of imaginary impedance (Z'') as a function of frequency for CZFTS. The resulting plots indicate a clear broadening of the peak towards higher frequencies with increasing temperature. Consequently, a temperature-dependent electrical relaxation phenomenon in the material is proposed [63]. The relaxation processes could be related to the presence of holes and/or vacancies at low temperatures and defects at higher temperatures. These peaks can be interpreted in terms of

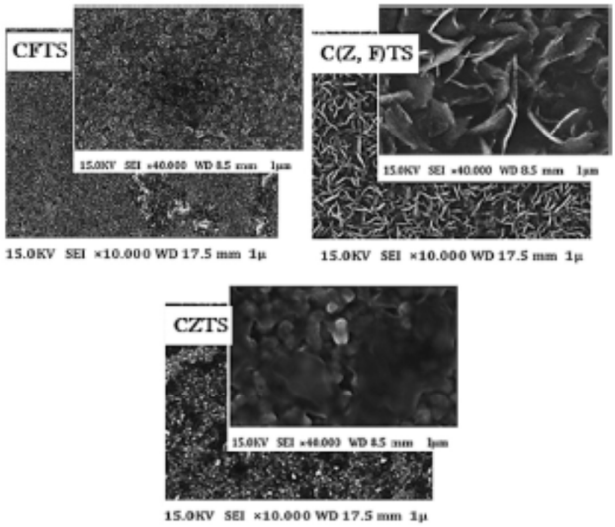

Fig. 8. Morphological FE-SEM images of $Cu_2Zn_xFe_{1-x}SnS_4$ thin films for x = 0, 0.5 and 1 (a and b represent the morphology of the $CZ_{0.5}F_{0.5}TS$ thin film at 40 K and 60 K magnification) and cross-sectional images of different films (a) CFTS, (b) $CZ_{0.5}F_{0.5}TS$ and (c) CZTS.

Table 6
Morphological and optical properties of CZFTS thin films.

Film	RMS (nm)	Thickness (nm) (obtained by the cross-sectional image)	Thickness (nm) (obtained by the profilometer)
Cu_2FeSnS_4	17 nm	220 ± 20	264 nm
$Cu_2Zn_{0.5}Fe_{0.5}SnS_4$	40 nm	320 ± 20	330 nm
Cu_2ZnSnS_4	47 nm	350 ± 20	370 nm

Arrhenius behaviour giving a measure of the activation energy. The relaxation time τ of these samples follows the Arrhenius law [64].

$$\omega_m = \omega_0 \exp(E_a / K_B T) \quad (6)$$

E_a is the activation energy and ω_0 is a constant. Therefore, as shown in Fig. 12, the expression of $Ln(\omega_m) = f(1000/T)$ leads to a linear function. The calculated values of 'E_a' are presented in Table 8.

The activation energy is the energy required for an ion to move from one site to another. In other words, it is the height of a potential barrier between two sites. The activation energy values of C(Z,F)TS thin films deposited on ordinary glass substrates have been previously evaluated [61]. This research revealed that for each material, the ions need two different activation energies to move from one site to another. In contrast, our study conducted under the same conditions as above for C(Z,F)TS deposited on intrinsic silicon substrates has the merit of reporting a single activation energy at each material with an improvement in the conductivity of these materials. Additionally, a slight decrease in Ea values can be noticed when the transition from C(F)TS to C(Z)TS takes place. Actually, the activation energy is closely related to the disorder in the material. Consequently, the activation energy increases as a function of the disorder and the more amorphous the material. However, the X-ray diffractograms of the CFTS layers show that the layers are less crystallized, which may explain why the activation energies are lower than those for the CZTS material. The Charge carrier transport properties, in particular holes, provide a better understanding of the electrical processes as a function of temperature and frequency. Fig. 13 shows the representative curve of $\ln\sigma_t$ versus $\ln(\omega)$ at different

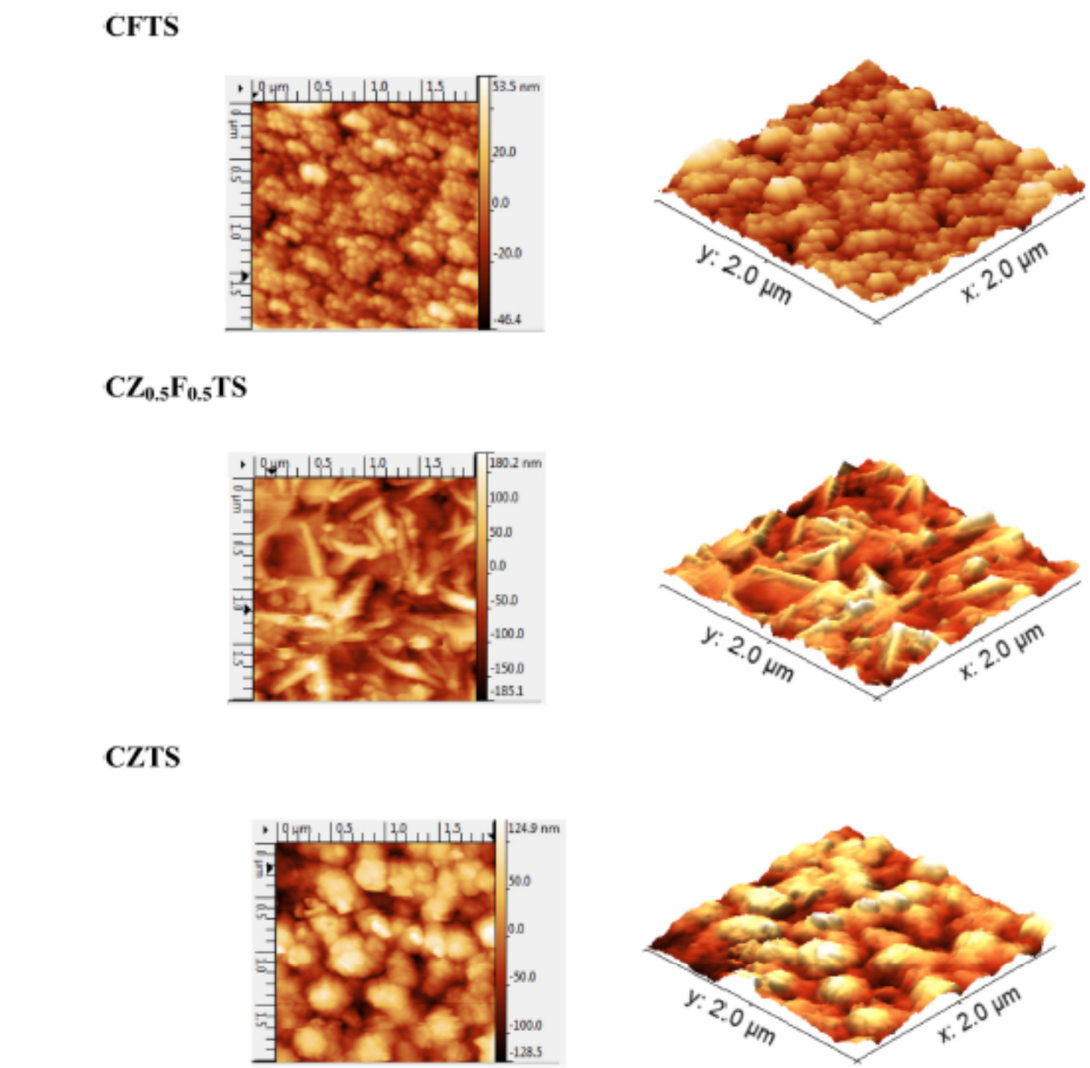

Fig. 9. 3D and 2D AFM images of (a) CFTS, (b) $CZ_{0.5}F_{0.5}TS$ and (c) CZTS thin films.

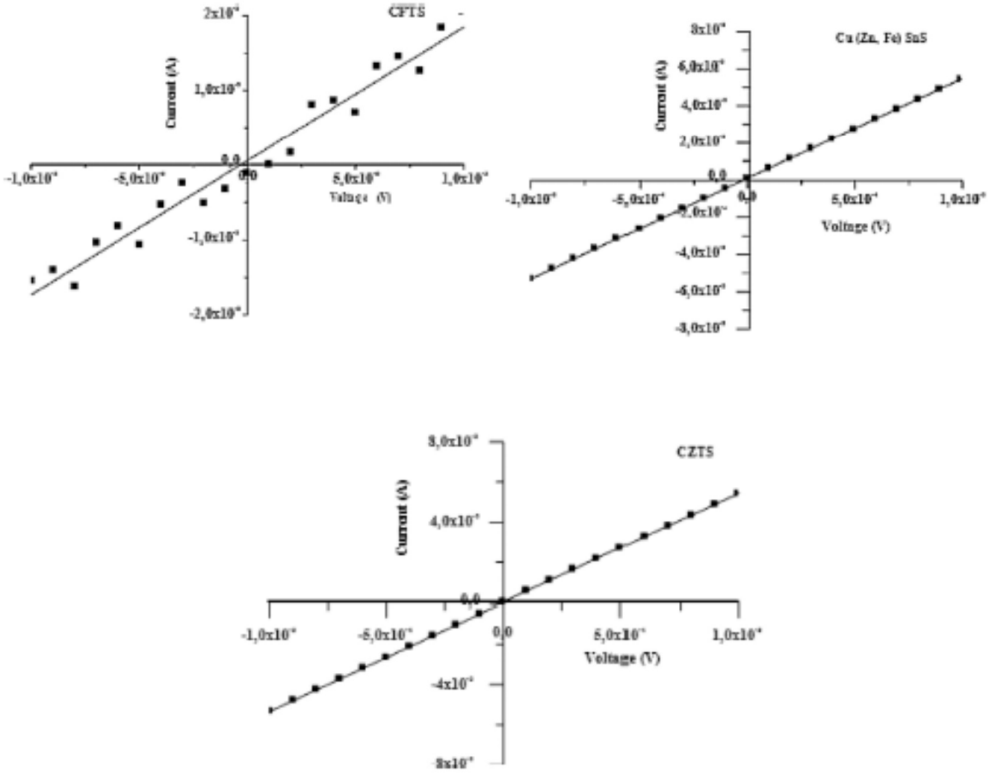

Fig. 10. Linear I–V plots of Silver past/CZFTS contacts.

Table 7
Electrical properties of C(Z, F)TS films estimated from the Hall measurements.

	Conductivity type	Carrier concentration (cm^{-3})	Resistivity (Ω. cm)	Mobility (cm^2/Vs)
CFTS	P	$5{,}5388 \times 10^{18}$	$2{,}5812 \times 10^{-3}$	$4{,}3661 \times 10^{2}$
$CZ_{0.5}F_{0.5}TS$	P	$2{,}2881 \times 10^{20}$	$1{,}0875 \times 10^{-2}$	2,5086
CZTS	P	$1{,}8837 \times 10^{18}$	$4{,}5230 \times 10^{-2}$	$7{,}3266 \times 10^{2}$

temperatures for CFTS, $Cu_2Zn_{0.5}Fe_{0.5}SnS_4$ and CZTS. The plot reveals two distinct regions:

- The low-frequency region in which the conductivity is not affected by the frequency. In this region, it can be seen that the conductivity increases with temperature, which indicates that the conduction mechanism is thermally activated.
- -The high frequencies where the increase in conductivity is linearly associated with frequency.

Fig. 13 depicts two distinct behavioral profiles that are consistent with the Jonscher model.

$$\sigma_{ac} + \sigma_{dc} = \sigma_t \tag{7}$$

$$\sigma_{dc} + A\omega^s = \sigma(\omega) \tag{8}$$

Where A is a component that evolves with temperature; "s" is the frequency coefficient. "s" is related to temperature and material characteristics and refers to the interactions between the lattice and individual free ions ($s \leq 1$).

It can be seen that all these curves show the same behavior. The conductivity at high frequencies increases with frequency and displays a marked shift in slope from the critical maximum angular pulsation ω_m, while at lower frequencies it is almost completely independent of frequency, which could be attributed to the contribution of the DC current. It also appears that the AC conductivity shifts to higher frequencies with temperature, which is consistent with the observed change in relaxation frequency. The observed shift therefore follows a thermally activated process. Furthermore, this frequency dependent conductivity is evidence for high frequency hopping conduction between localized states [65].

The slopes ''s'' of the $\ln(\sigma_{AC})$ and $\ln(\omega)$ curves at different temperatures have been calculated [66,67]. This parameter ''s'' is considered to be related to the interaction between all charge species involved in the polarization process [66,67], it is used to describe the AC component contributing to the dispersive region [66,67]. The obtained values of ''s'' were found to be less than unity and correspond to extrinsic dipolar charge carriers from defects and impurities in the film [68,69]. The frequency dependence of conductivity is an indication of the conduction through high frequency jumps between localized states [70,71].

The conduction mechanism is established by exploiting the obtained values of the parameter "s". Following CBH model, the charge carriers cross a potential barrier that separates the different sites [72,73]. Furthermore, we note that the exponent decreases with increasing temperature and presents a straight curve, which is consistent with the Elliott model [73,74].

4. Conclusions

This paper reports the synthesis of $Cu_2Zn_xFe_{1-x}SnS_4$ thin films

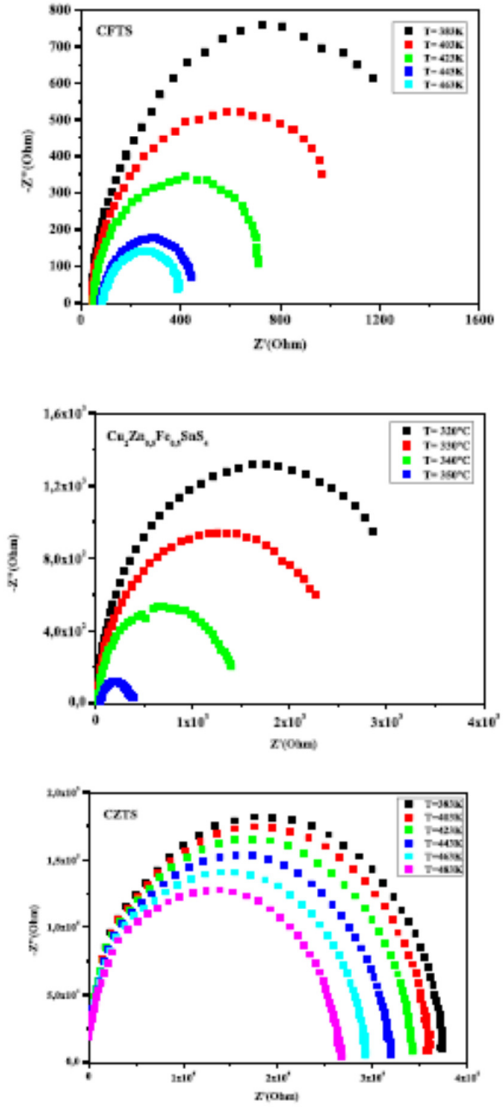

Fig. 11. Complex impedance spectra of CZFTS materials as a function of the annealing temperature.

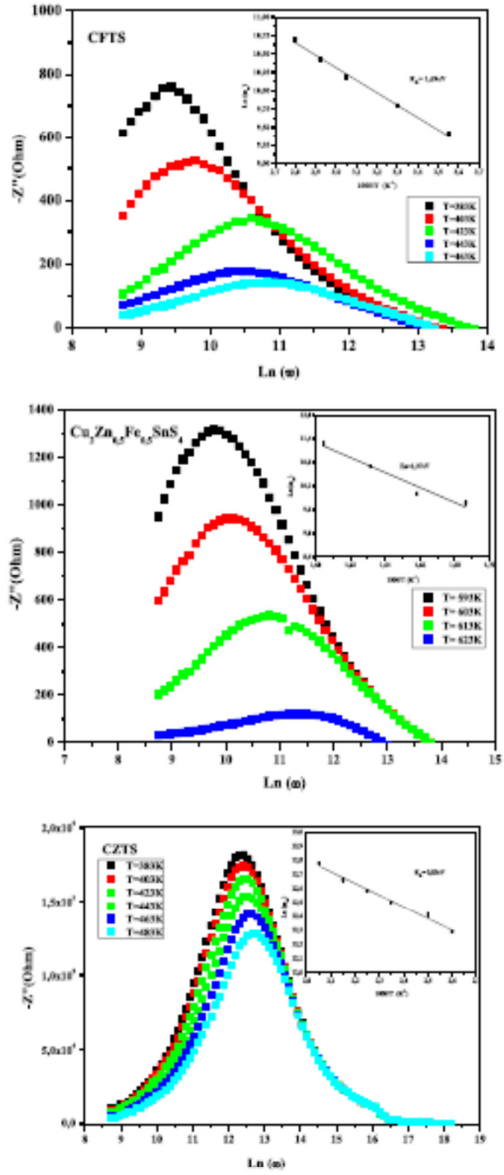

Fig. 12. Angular frequency dependence of Z'' at different temperatures, insets show variation of the activation energy as a function of the temperature.

deposited on intrinsic silicon substrates: Cu_2FeSnS_4, $Cu_2Zn_{0.5}Fe_{0.5}SnS_4$ and Cu_2ZnSnS_4 were successfully synthesized by a solid-state reaction method. Structural analysis by X-ray diffraction revealed that all the CZFTS powders were polycrystalline with a preferential orientation along the (112) plane. A structural transition from stannite (x = 0) to kesterite (x = 1) can be observed with increasing zinc content. EDS analysis showed that the compositions obtained from the synthesized powders were very close to the expected theoretical stoichiometry. CZFTS thin films deposited on intrinsic silicon by thermal evaporation in vacuum and then sulphided under nitrogen flow at 400 °C. Structural analysis indicates that they are polycrystalline with a preferential orientation along the (112) plane. Morphological studies show the increase in grain size and thickness of the thin films as a function of Zn content caused by this crystallographic change. Electrical analysis by the hot tip method indicates p-type behavior for CZFTS. Hall measurements

Table 8
Activation energy values obtained for C(Z, F)TS.

Material's	Ea (eV)
Cu_2FeSnS_4	1.69
$Cu_2Zn_{0.5}Fe_{0.5}SnS_4$	1.37
Cu_2ZnSnS_4	0.83

show that CZTS has the best carrier mobility and the lowest resistivity values. The impedance spectroscopy study shows that the electrical characteristics are strongly temperature dependent. The frequency exponent values ''s'' suggest that the correlated barrier hopping (CBH)

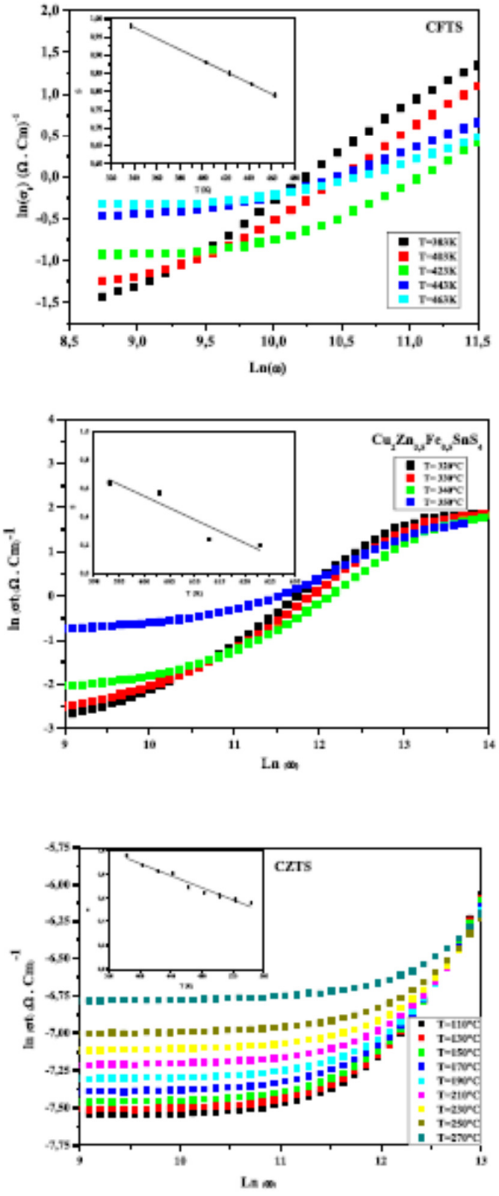

Fig. 13. Angular frequency dependence of AC conductivity at different temperatures. Inset shows variation of the "s" parameter as a function of the annealing temperature.

model is the most appropriate model to characterize the electrical conduction mechanism of the obtained $Cu_2Zn_xFe_{1-x}SnS_4$ thin films. In conclusion, the CZFTS compound could be suitable for application as absorber layer in solar cell.

CRediT authorship contribution statement

Marwa Sebaï: Investigation, Methodology, Writing – original draft. **Jean-Louis Lazzari:** Supervision, Visualization. **Mounir Kanzari:** Supervision, Validation.

Declaration of Competing Interest

The authors declare that they have no known competing financial interests or personal relationships that could have appeared to influence the work reported in this paper.

Data availability

The authors are unable or have chosen not to specify which data has been used.

References

[1] M.I. Hoffert, K. Caldeira, A.K. Jain, E.F. Haites, L.D.D. Harvey, S.D. Potter, M. E. Schlesinger, S.H. Schneider, R.G. Watts, T.M.L. Wigley, D.J. Wuebbles, Energy implications of future stabilization of atmospheric CO_2 content, Nature 395 (1998) 881–884, https://doi.org/10.1038/27638.

[2] R. Joshi, M. Pathak, Decentralized grid-connected power generation potential in India: from perspective of energy efficient buildings, Energy Procedia 57 (2014) 716–724, https://doi.org/10.1016/j.egypro.2014.10.227.

[3] R. Kamada, T. Yagioka, S. Adachi, A. Handa, K.F. Tai, T. Kato, H. Sugimoto, New world record Cu(In, Ga)(Se, S)<inf>2</inf> thin film solar cell efficiency beyond 22%, in: Proceedings of the Forty Third Photovolt. Spec. Conf., IEEE, 2016, 1287–1291. https://doi.org/10.1109/PVSC.2016.7749822.

[4] Z. Shadrokh, A. Yazdani, H. Eshghi, Solvothermal synthesis of Cu2Zn1−xFexSnS4 nanoparticles and the influence of annealing conditions on drop-casted thin films, Semicond. Sci. Technol. 31 (2016), 045004.

[5] Z. Shadrokh, A. Yazdani, H. Eshghi, Solvothermal synthesis of $Cu_2Zn_{1-x}Fe_xSnS_4$ nanoparticles and the influence of annealing conditions on drop-casted thin films, Semicond. Sci. Technol. 31 (2016), 045004, https://doi.org/10.1088/0268-1242/31/4/045004.

[6] D.B. Khadka, J. Kim, Structural transition and band gap tuning of $Cu_2(Zn,Fe)SnS_4$ chalcogenide for photovoltaic application, J. Phys. Chem. C 118 (2014) 14227–14237, https://doi.org/10.1021/jp503678h.

[7] H. Hussein, A. Yazdani, Investigation the influence of Fe (III) doping in Cu2ZnSnS4 semiconductor: structural, optical and magnetic properties, Optik 179 (2019) 505–513, https://doi.org/10.1016/j.ijleo.2018.10.138.

[8] S.R. Hall, J.T. Szymanski, J.M. Stewart, Kesterite, Cu2 (Zn,Fe)SnS4, and stannite, Cu2 (Fe,Zn)SnS4, structurally similar but distinct minerals, Can. Mineral. (1978).

[9] Kentaro Ito, ed., Copper Zinc Tin Sulfide-Based Thin-Film Solar Cells, John Wiley & Sons, Ltd, Hoboken USA, 2014.

[10] W. Wang, M.T. Winkler, O. Gunawan, T. Gokmen, T.K. Todorov, Y. Zhu, D.B. Mitzi, Device characteristics of CZTSSe thin-film solar cells with 12.6% efficiency, Adv. Energy Mater. 4 (2014), 1301465, https://doi.org/10.1002/aenm.201301465.

[11] R.R. Prabhakar, N. Huu Loc, M.H. Kumar, P.P. Boix, S. Juan, R.A. John, S. K. Batabyal, L.H. Wong, Facile water-based spray pyrolysis of earth-abundant Cu_2FeSnS_4 thin films as an efficient counter electrode in dye-sensitized solar cells, ACS Appl. Mater. Interfaces 6 (2014) 17661–17667, https://doi.org/10.1021/am503888v.

[12] C. Huang, Y. Chan, F. Liu, D. Tang, J. Yang, Y. Lai, J. Li, Y. Liu, Synthesis and characterization of multicomponent Cu2(FexZn1−x)SnS4 nanocrystals with tunable band gap and structure, J. Mater. Chem. A 1 (2013) 5402, https://doi.org/10.1039/c3ta00191a.

[13] T. Shibuya, Y. Goto, Y. Kamihara, M. Matoba, K. Yasuoka, L.A. Burton, A. Walsh, From kesterite to stannite photovoltaics: stability and band gaps of the $Cu_2(Zn,Fe)SnS_4$ alloy, Appl. Phys. Lett. 104 (2014), 021912, https://doi.org/10.1063/1.4862030.

[14] A. Hannachi, H. Ouslati, N. Khemiri, M. Kanzari, Effects of sulfurization on the optical properties of Cu2ZnxFe1-xSnS4 thin films, Opt. Mater. 72 (2017) 702–709, https://doi.org/10.1016/j.optmat.2017.07.031.

[15] V. Trifiletti, G. Tseberlidis, M. Colombo, A. Spinardi, S. Luong, M. Danilson, M. Grossberg, O. Fenwick, S. Binetti, Growth and characterization of Cu2ZnI−xFexSnS4 thin films for photovoltaic applications, Materials 13 (2020) 1471, https://doi.org/10.3390/ma13061471.

[16] B. Bibi, B. Farhadi, W. ur Rahman, A. Liu, A novel design of CTZS/Si tandem solar cell: a numerical approach, J. Comput. Electron. 20 (2021) 1769–1778, https://doi.org/10.1007/s10825-021-01733-4.

[17] A. Hannachi, N. Khemiri, M. Kanzari, Influence of Fe/Zn content on the structural, and optical properties of nontoxic and earth-abundant Cu2ZnxFe1 − xSnS4 (x = 0, 0.25, 0.5, 0.75 and 1) compounds, J. Mater. Sci. Mater. Electron. 33 (2022) 20604–20615, https://doi.org/10.1007/s10854-022-08872-9.

[18] S. Mahjoubi, N. Bitri, H. Bouzouita, M. Abaab, I. Ly, Effect of the annealing and the spraying time on the properties of CZTS thin films prepared by the "Spray sandwich" technique, Appl. Phys. A 123 (2017) 452, https://doi.org/10.1007/s00339-017-1020-4.

[19] D.B. Khadka, J. Kim, Structural transition and band gap tuning of $Cu_2(Zn,Fe)SnS_4$ chalcogenide for photovoltaic application, J. Phys. Chem. C 118 (2014) 14227–14237, https://doi.org/10.1021/jp503678h.

[20] Z. Shadrokh, A. Yazdani, H. Eshghi, Solvothermal synthesis of Cu 2 Zn 1− x Fe x SnS 4 nanoparticles and the influence of annealing conditions on drop-casted thin films, Semicond. Sci. Technol. 31 (2016), 045004, https://doi.org/10.1088/0268-1242/31/4/045004.

[21] R.G. Crespo, S. Hamad, C.R.A. Catlow, N.H. de Leeuw, Symmetry-adapted configurational modelling of fractional site occupancy in solids, J. Phys. Condens. Matter 19 (2007), 256201, https://doi.org/10.1088/0953-8984/19/25/256201.
[22] S. Siebentritt, S. Schorr, Kesterites-a challenging material for solar cells, Prog. Photovolt. Res. Appl. 20 (2012) 512–519, https://doi.org/10.1002/pip.2156.
[23] B.N. Schumer, R.T. Downs, K.J. Domanik, M.B. Andrade, M.J. Origlieri, Pirquitasite, Ag 2 ZnSnS4, Acta Crystallogr. Sect. E Struct. Rep. Online 69 (2013) i8–i9, https://doi.org/10.1107/S1600536813001013.
[24] S. Schorr, H.J. Hoebler, M. Tovar, A neutron diffraction study of the stannite-kesterite solid solution series, Eur. J. Mineral. 19 (n.d.) 65–73.
[25] T. Shibuya, Y. Goto, Y. Kamihara, M. Matoba, K. Yasuoka, L. A.Burton, A. Walsh, From kesterite to stannite photovoltaics: stability and band gaps of the Cu2(Zn,Fe)SnS4 alloy, Appl. Phys. Lett. 104 (2014), 021912, https://doi.org/10.1063/1.4862030.
[26] C. Yan, C. Huang, J. Yang, F. Liu, J. Liu, Y. Lai, J. Li, Y. Liu, Synthesis and characterizations of quaternary Cu2FeSnS4 nanocrystals, Chem. Commun. 48 (2012) 2603, https://doi.org/10.1039/c2cc16972j.
[27] P. Scherrer, Bestimmung der Größe und der inneren Struktur von Kolloidteilchen mittels Röntgenstrahlen, iNhrichten von der Gesellschaft der Wissenschaften zu Göttingen, 26, 1918.
[28] W. Wang, H. Shen, J. Chen, W. Chen, X. He, Synthesis and properties of Cu2(FexZn1−x)SnS4 nanocrystals by microwave irradiation assisted solvothermal method, Adv. Powder Technol. 26 (2015) 275–279, https://doi.org/10.1016/j.apt.2014.10.009.
[29] A. Akkari, M. Reghima, C. Guasch, N. Kamoun-Turki, Effect of copper doping on physical properties of nanocrystallized SnS zinc blend thin films grown by chemical bath deposition, J. Mater. Sci. 47 (2012) 1365–1371, https://doi.org/10.1007/s10853-011-5912-y.
[30] G.K. Williamson, R.E. Smallman, III. Dislocation densities in some annealed and cold-worked metals from measurements on the X-ray debye-scherrer spectrum, Philos. Mag. 1 (1956) 34–46, https://doi.org/10.1080/14786435608238074.
[31] JCPDS card No. 00-036-1450.
[32] JCPDS card No. 01-089-2028.
[33] JCPDS card No. 00-039-0354.
[34] J.I. Langford, A.J.C. Wilson, Scherrer after sixty years: a survey and some new results in the determination of crystallite size, J. Appl. Crystallogr 11 (1978) 102–113, https://doi.org/10.1107/S0021889878012844.
[35] S. Ray, R. Banerjee, A.K. Barua, Properties of vacuum-evaporated CdS thin films, Jpn. J. Appl. Phys. 19 (1980) 1889–1895, https://doi.org/10.1143/JJAP.19.1889.
[36] S. Prabahar, M. Dhanam, CdS thin films from two different chemical baths—structural and optical analysis, J. Cryst. Growth 285 (2005) 41–48, https://doi.org/10.1016/j.jcrysgro.2005.08.008.
[37] H. Oueslati, M. Ben Rabeh, M. Kanzari, Synthesis and characterization of next generation Cu2ZnxFe1−xSnS4 (x = 0, 0.25, 0.5, 0.75 and 1) compounds, J. Electron. Mater. 49 (2020) 627–636, https://doi.org/10.1007/s11664-019-07766-7.
[38] X. Jiang, W. Xu, R. Tan, W. Song, J. Chen, Solvothermal synthesis of highly crystallized quaternary chalcogenide Cu2FeSnS4 particles, Mater. Lett. 102–103 (2013) 39–42, https://doi.org/10.1016/j.matlet.2013.03.102.
[39] Fabiana Meijon Fadul, Polarization dependent Raman spectroscopy characterization of kesterite Cu2ZnSnS4 single crystals, 1538 (2019) 95–101. DOI: 1 557/op 013 0.1 l.2.1015.
[40] M. Dimitrievska, A. Fairbrother, X. Fontané, T. Jawhari, V. Izquierdo-Roca, E. Saucedo, A. Pérez-Rodríguez, Multiwavelength excitation Raman scattering study of polycrystalline kesterite Cu_2ZnSnS_4 thin films, Appl. Phys. Lett. 104 (2014), https://doi.org/10.1063/1.4861593.
[41] M. Himmrich, H. Haeuseler, Far infrared studies on stannite and wurtzstannite type compounds, Spectrochim. Acta Part A Mol. Spectrosc. 47 (1991) 933–942, https://doi.org/10.1016/0584-8539(91)80283-O.
[42] A.-J. Cheng, M. Manno, A. Khare, C. Leighton, S.A. Campbell, E.S. Aydil, Imaging and phase identification of Cu_2ZnSnS_4 thin films using confocal Raman spectroscopy, J. Vac. Sci. Technol. A Vac., Surf. Film. 29 (2011), 051203, https://doi.org/10.1116/1.3625249.
[43] A. Khare, B. Himmetoglu, M. Cococcioni, E.S. Aydil, First principles calculation of the electronic properties and lattice dynamics of Cu2ZnSn(S 1-xSe x)4, J. Appl. Phys. 111 (2012), https://doi.org/10.1063/1.4728232.123704.
[44] T. Gürel, C. Sevik, T. Çağın, Characterization of vibrational and mechanical properties of quaternary compounds Cu2ZnSnS4 and Cu2ZnSnSe4 in kesterite and stannite structures, Phys. Rev. B Condens. Matter Mater. Phys. 84 (2011) 1–7, https://doi.org/10.1103/PhysRevB.84.205201.
[45] G.L. Agawane, S.W. Shin, S.A. Vanalakar, A.V. Moholkar, J.H. Kim, Next generation promising Cu2(ZnxFe1−x)SnS4 photovoltaic absorber material prepared by pulsed laser deposition technique, Mater. Lett. 137 (2014) 147–149, https://doi.org/10.1016/j.matlet.2014.08.118.
[46] Yousef Alghamdi, The AACVD of CFTS Family of Materials, International Journal of Advanced Research in Chemical Science, 2017.
[47] K. Tanaka, Y. Fukui, N. Moritake, H. Uchiki, Chemical composition dependence of morphological and optical properties of Cu2ZnSnS4 thin films deposited by sol–gel sulfurization and Cu2ZnSnS4 thin film solar cell efficiency, Sol. Energy Mater. Sol. Cells 95 (2011) 838–842, https://doi.org/10.1016/j.solmat.2010.10.031.
[48] C.S. Kanuru, G.L. Shekar, L. Krishnamurthy, R. Gopal Krishne Urs, Surface morphological studies of solar absorber layer Cu2ZnSnS4(CZTS) thin films by non-vacuum deposition methods, J. Nano Electron. Phys. 6 (2014) 2077–6072.
[49] D.B. Khadka, J. Kim, Structural, optical and electrical properties of Cu2FeSnX4 (X = S, Se) thin films prepared by chemical spray pyrolysis, J. Alloy. Compd. 638 (2015) 103–108, https://doi.org/10.1016/j.jallcom.2015.03.053.
[50] C. Nefzi, M. Souli, Y. Cuminal, N. Kamoun-Turki, Effect of sulfur concentration on structural, optical and electrical properties of Cu2FeSnS4 thin films for solar cells and photocatalysis applications, Superlattices Microstruct. 124 (2018) 17–29, https://doi.org/10.1016/j.spmi.2018.09.033.
[51] S. Chen, A. Walsh, X.-G. Gong, S.-H. Wei, Classification of lattice defects in the Kesterite Cu(2) ZnSnS(4) and Cu(2) ZnSnSe(4) earth-abundant solar cell absorbers, Adv. Mater. 25 (2013) 1522–1539, https://doi.org/10.1002/adma.201203146.
[52] E. García-Hemme, A. Fairbrother, L. Calvo-Barrio, E. Saucedo, I. Martil, Compositional dependence of chemical and electrical properties in Cu2ZnSnS4 thin films, IEEE J. Photovolt. 6 (2016) 990–996, https://doi.org/10.1109/JPHOTOV.2016.2566888.
[53] U. Syafiq, N. Ataollahi, R.D. Maggio, P. Scardi, Solution-based synthesis and characterization of Cu 2 ZnSnS 4 (CZTS) thin films, Molecules 24 (2019) 3454, https://doi.org/10.3390/molecules24193454.
[54] M.M. Öztaş, Influence of grain size on electrical and optical properties of InP films, Chin. Phys. Lett. 25 (2008) 4090–4092, https://doi.org/10.1088/0256-307X/25/11/069.
[55] S.W. Shin, S.M. Pawar, C.Y. Park, J.H. Yun, J.H. Moon, J.H. Kim, J.Y. Lee, Studies on Cu2ZnSnS4 (CZTS) absorber layer using different stacking orders in precursor thin films, Sol. Energy Mater. Sol. Cells 95 (2011) 3202–3206, https://doi.org/10.1016/j.solmat.2011.07.005.
[56] F. Goumrhar, L. Bahmad, O. Mounkachi, A. Benyoussef, Ab initio calculations of the magnetic properties of TM (Ti, V)-doped zinc-blende ZnO, Int. J. Mod. Phys. B 31 (2017) 1850025–1850037, https://doi.org/10.1142/s0217979218500254.
[57] A. Ait. Raiss, Y. Sbai, L. Bahmad, A. Benyoussef, Magnetic and magneto-optical properties of doped and co-doped CdTe with (Mn, Fe): Ab-initio study, J. Magn. Magn. Mater. 385 (2015) 295–301, https://doi.org/10.1016/j.jmmm.2015.02.077.
[58] S. Idrissi, H. Labrim, L. Bahmad, A. Benyoussef, DFT and TDDFT studies of the new inorganic perovskite CaPbI3 for solar cell applications, Chem. Phys. Lett. 766 (2021), 138347, https://doi.org/10.1016/j.cplett.2021.138347.
[59] S. Idrissi, L. Bahmad, A. Benyoussef, DFT and TDDFT studies of structural, electronic and optical properties of the inorganic solar perovskites XPbBr3 (X = Li or Na), Philos. Transit 95 (2022) 501–514, https://doi.org/10.1080/01411594.2022.2080064.
[60] I. Trabelsi, A. Jebali, M. Kanzari, Electrical characterization of SnSb4S7 thin films by impedance spectroscopy, J. Mater. Sci. Mater. Electron. 27 (2016) 4326–4335, https://doi.org/10.1007/s10854-016-4300-4.
[61] M. Sebai, I. Trabelsi, M. Kanzari, Comparative study of electrical properties of Cu2ZnxFe1−xSnS4 thin films, Mater. Sci. Eng. B 240 (2019) 55–61, https://doi.org/10.1016/j.mseb.2019.01.004.
[62] K. Prabakar, S.K. Narayandass, D. Mangalaraj, Dielectric studies on Cd0.4Zn0.6Te thin films, Mater. Chem. Phys. 78 (2003) 809–815, https://doi.org/10.1016/S0254-0584(02)00388-7.
[63] S.K. Barik, P.K. Mahapatra, R.N.P. Choudhary, Structural and electrical properties of Na1/2La1/2TiO3 ceramics, Appl. Phys. A 85 (2006) 199–203, https://doi.org/10.1007/s00339-006-3668-z.
[64] A. Larbi, I. Trabelsi, H. Dahman, M. Kanzari, Investigation on the AC and DC electrical conductivity of Sn3Sb2S6 thin films prepared by glancing angle deposition, J. Mater. Sci. Mater. Electron. 29 (2018) 2907–2914, https://doi.org/10.1007/s10854-017-8221-7.
[65] R. Ondo-Ndong, G. Ferblantier, F. Pascal-Delannoy, A. Boyer, A. Foucaran, Electrical properties of zinc oxide sputtered thin films, Microelectron. J. 34 (2003) 1087–1092, https://doi.org/10.1016/S0026-2692(03)00198-8.
[66] N.D. Sankir, E. Aydın, M. Sankir, Impedance spectroscopy and dielectric properties of silver incorporated indium sulfide thin films, Int. J. Electrochem. Sci. 9 (2014) 3864–3875.
[67] Nevill Francis Mott, Edward A. Davis, Electronic processes in non-crystalline materials, Oxf. Class. Texts Phys. Sci. (1979).
[68] S.S.N. Bharadwaja, P. Victor, P. Venkateswarulu, S.B. Krupanidhi, AC transport studies of La-modified antiferroelectric lead zirconate thin films, Phys. Rev. B 65 (2002), 174106, https://doi.org/10.1103/PhysRevB.65.174106.
[69] P. Venkateswarlu, A. Laha, S.B. Krupanidhi, AC properties of laser ablated La-modified lead titanate thin films, Thin Solid Films 474 (2005) 1–9, https://doi.org/10.1016/j.tsf.2004.02.101.
[70] A. Mhamdi, B. Ouni, A. Amlouk, K. Boubaker, M. Amlouk, Study of nickel doping effects on structural, electrical and optical properties of sprayed ZnO semiconductor layers, J. Alloy. Compd. 582 (2014) 810–822, https://doi.org/10.1016/j.jallcom.2013.08.080.
[71] S. Ojha, M.S. Ali, M. Roy, S. Bhattacharya, Hopping frequency and conductivity relaxation of promising chalcogenides: AC conductivity and dielectric relaxation approaches, Mater. Res. Express 8 (2021), 085203, https://doi.org/10.1088/2053-1591/ac1d17.
[72] J.T. Gudmundsson, H.G. Svavarsson, S. Gudjonsson, H.P. Gislason, Frequency-dependent conductivity in lithium-diffused and annealed GaAs, Phys. B Condens. Matter 340–342 (2003) 324–328, https://doi.org/10.1016/j.physb.2003.09.082.
[73] K. Ebnalwaled, Hopping conduction and dielectric properties of InSb bulk crystal, Int. J. Basic Appl. Sci. 11 (2011) 194–207.
[74] S.R. Elliott, A theory of a.c. conduction in chalcogenide glasses, Philos. Mag. 36 (1977) 1291–1304, https://doi.org/10.1080/14786437708238517.